International Journal of Extreme Manufacturing

In-situ structural evolution of Bi_2O_3 nanoparticle catalysts for CO_2 electroreduction

OPEN ACCESS
IOP Publishing | IMMT
International Journal of Extreme Manufacturing
Int. J. Extrem. Manuf. 4 (2022) 035002 (8pp)
https://doi.org/10.1088/2631-7990/ac7a6e

In-situ structural evolution of Bi_2O_3 nanoparticle catalysts for CO_2 electroreduction

Hongbo Wang[1], Chongyang Tang[1], Bo Sun[1], Jiangchao Liu[1], Yan Xia[1], Wenqing Li[1], Changzhong Jiang[1], Dong He[1,*] and Xiangheng Xiao[1,2,*]

[1] Department of Physics, Hubei Nuclear Solid Physics Key Laboratory, Wuhan University, Wuhan 430072, People's Republic of China
[2] Hubei Yangtze Memory Laboratories, Wuhan 430205, People's Republic of China

E-mail: hedong@whu.edu.cn and xxh@whu.edu.cn

Received 17 January 2022, revised 12 April 2022
Accepted for publication 20 June 2022
Published 1 July 2022

Abstract

Under the complex external reaction conditions, uncovering the true structural evolution of the catalyst is of profound significance for the establishment of relevant structure–activity relationships and the rational design of electrocatalysts. Here, the surface reconstruction of the catalyst was characterized by *ex-situ* methods and *in-situ* Raman spectroscopy in CO_2 electroreduction. The final results showed that the Bi_2O_3 nanoparticles were transformed into Bi/Bi_2O_3 two-dimensional thin-layer nanosheets (NSs). It is considered to be the active phase in the electrocatalytic process. The Bi/Bi_2O_3 NSs showed good catalytic performance with a Faraday efficiency (FE) of 94.8% for formate and a current density of 26 mA cm^{-2} at −1.01 V. While the catalyst maintained a 90% FE in a wide potential range (−0.91 V to −1.21 V) and long-term stability (24 h). Theoretical calculations support the theory that the excellent performance originates from the enhanced bonding state of surface Bi-Bi, which stabilized the adsorption of the key intermediate OCHO* and thus promoted the production of formate.

Supplementary material for this article is available online

Keywords: CO_2 electroreduction, structural evolution, electrocatalysis, interface, formic acid

1. Introduction

In recent years, the conversion and utilization of renewable energy have become particularly significant for making progress in environmental and energy sustainable development [1]. However, the use of wind and solar energy with intermittent characteristics will lead to high electricity storage costs [2]. Electrocatalytic CO_2 reduction reaction (CO_2RR) technology to convert the greenhouse gas CO_2 into value-added products for carbon neutrality and energy storage has received considerable attention [3–5]. Among the various products of CO_2RR, the liquid product formic acid has been noticeable. Formic acid is not only an important raw material in chemical production but also can be used as an excellent hydrogen storage material, and it also has wide application potential in fuel cells [6, 7]. This makes formic acid/formate one of the most competitive high-value products among the many products of CO_2RR. However, due to the chemical inertness of the CO_2 molecules and the strong competition with hydrogen evolution reaction (HER), both the product selectivity and the activity of existing catalysts are not satisfactory [8].

* Authors to whom any correspondence should be addressed.

Although noble metal-based catalysts have good catalytic performance in formic acid production, their high toxicity or rarity hinders the development of commercialization. Recent studies have suggested that cheap metals represented by Sn and Bi were more widely used in the conversion of CO_2 to formic acid [9]. However, the poor formic acid selectivity of Sn-based catalysts has impeded its further development. In contrast, bismuth-based catalysts were more commonly used in CO_2RR, and huge progress has been made because of their large reserves, green pollution-free characteristics [10–13].

With the further progress of the CO_2RR research, researchers gradually realized that such metal compounds underwent dynamic structural evolution in the reduction process, which could lead to the uncertainty of active species. The structural evolution of the catalyst in the reaction was affected by external potential, electrolytes, and other factors [14–16]. Previous studies have demonstrated that the surface of InN nanosheets (NSs) was reconstructed in the CO_2RR, which hugely affected the catalytic activity of the catalyst [17]. For Bi-based oxides, the dynamic evolution of catalysts at cathodic potential still remains unclear. The CO_2RR performance of the reported Bi NSs with the *in-situ* topological transformation of BiOI NSs was excellent [18]. Compared to the zero-valent Bi metal, the presence of oxygen species in the real reaction environment and the potential role of possible metal/metal oxide evolution configuration in the CO_2 reduction process were rarely taken into account [19–23]. More importantly, the micromorphology and structure of the catalyst were greatly restricted by external environmental conditions [24, 25]. There is an urgent need to employ the *in-situ* spectroscopic characterizations to track its real evolution process [26–28] and assist in establishing a real active structure model. The above is of great significance for the study of the structure–activity relationship and determining the reaction active sites in the CO_2RR system.

In this paper, cubic phase Bi_2O_3 nanoparticles (NPs), Bi NPs, and Bi_2O_3 NSs were synthesized by solvothermal method or subsequent thermal annealing. The *ex-situ* analysis demonstrated that the surface of Bi_2O_3 NPs was reconstructed to generate Bi nanocrystals embedded on two-dimensional (2D) Bi_2O_3 NSs. The *In-situ* Raman test demonstrated the reconstruction process, and the Bi–O vibration of Bi_2O_3 can always be found in the electroreduction progress. The final Bi/Bi_2O_3 structure plays a more effective role in promoting CO_2RR. At −1.01 V vs. reversible hydrogen electrode (RHE), the maximum FE of formate was close to 94.8%, and FE of formate can be maintained at around 90% over a wide potential window from −0.91 V to −1.21 V vs. RHE. Moreover, the catalyst can be maintained in good reaction stability (24 h). Density functional theory (DFT) results indicated that the electrochemical reconstruction process can lead to the charge redistribution, especially when the presence of the Bi_2O_3 substrate provides more electrons that can be transported to the vicinity of the surface Bi layer. This enhances the bonding strength and helps to form a stable electron-rich Bi metal layer. It optimizes the activation behavior of CO_2 molecules and reduces the energy barrier of subsequent the OCHO* intermediates, which ultimately greatly promotes the production of formate. The above is of great significance to guide the rational design of catalysts with more stable and excellent performance.

2. Results and discussion

As shown in figure 1(a), Bi_2O_3 NPs were synthesized by a simple hydrothermal method. Both scanning electron microscope (SEM) and transmission electron microscope (TEM) found that the particle size of the synthesized Bi_2O_3 NPs was in the range of 50–100 nm (figure S1). The high-resolution TEM (HRTEM) (figure 1(b)) gave the information that the 0.28 nm and 0.31 nm interplanar spacings matched with (200) and (111) planes of cubic Bi_2O_3 respectively. X-ray diffraction (XRD) supported the result that the diffraction peaks at 27.95°, 32.38°, 46.45°, and 55.08° on Bi_2O_3 NPs corresponded to the (1 1 0), (2 0 0), (2 2 0) and (3 1 1) planes of cubic Bi_2O_3 (JCPDS, No. 74-1373) (figure S2). The dispersed Bi_2O_3 NPs were uniformly loaded into carbon paper as the working electrode. After a brief electrochemical reconstruction process at the cathode potential, XRD (figure 1(c)) indicated the appearance of the metallic Bi phase (JCPDS, No. 85-1331), and the Bi_2O_3 NPs were transformed into 2D NSs embedded with Bi nanocrystals (figures 1(d) and S3). The interplanar spacings of 0.38 nm and 0.33 nm in the calibrated Bi nanocrystals corresponded to the (101) and (012) planes of diamond Bi respectively (figures 1(e) and (f)). Characteristically, a fast Fourier transform filter also showed a diffraction pattern with six-fold symmetry. The 0.28 nm lattice fringe can be allocated to the (200) plane of Bi_2O_3, and the thickness of the generated NSs is only 4–6 nm (figure 1(g)). SEM–energy dispersive x-ray spectroscopy (SEM–EDS) method (figures S4 and S5) also showed an increase in the ratio of elemental Bi/O.

With the aim of reflecting the dynamic evolution of the catalyst surface during the CO_2RR process, Bi_2O_3 NPs, Bi NPs, and Bi_2O_3 NSs were tested by the *in-situ* Raman detection (figure S6). A low-energy 633 nm laser (light intensity: strength 5%) excited by He–Ne laser was used to eliminate laser oxidation caused by thermal effect [29]. In the open circuit potential, the Bi_2O_3 NPs had two low-frequency stretching vibrations Raman peaks at 65 and 167 cm^{-1} [30, 31]. After applying the bias voltage, the peak at 65 cm^{-1} was gradually replaced by the new peaks at 71 and 98 cm^{-1}, which were consistent with the typical two first-order optical bands pattern of metal Bi [32]. The peak at 167 cm^{-1}, although attenuated, still remained exist and then increased slightly after removing the potential. Significant change of the Roman Peak was not found with the extension of reaction time (figure 2(a)). The continuous maintenance of Bi–O vibrations was also verified by Raman spectroscopy after standard electrochemical testing time (2 h) (figure S7). Then, the test was repeated by applying different potentials within the potential window used immediately, resulting in close peak positions (figure 2(b)). Furthermore, the *in-situ* Raman results of Bi NPs exposed that the intensity of Bi Raman peak remained stable regardless of the change of applied potential or the extension of cathode time (figure S8), and the particles slightly aggregated under

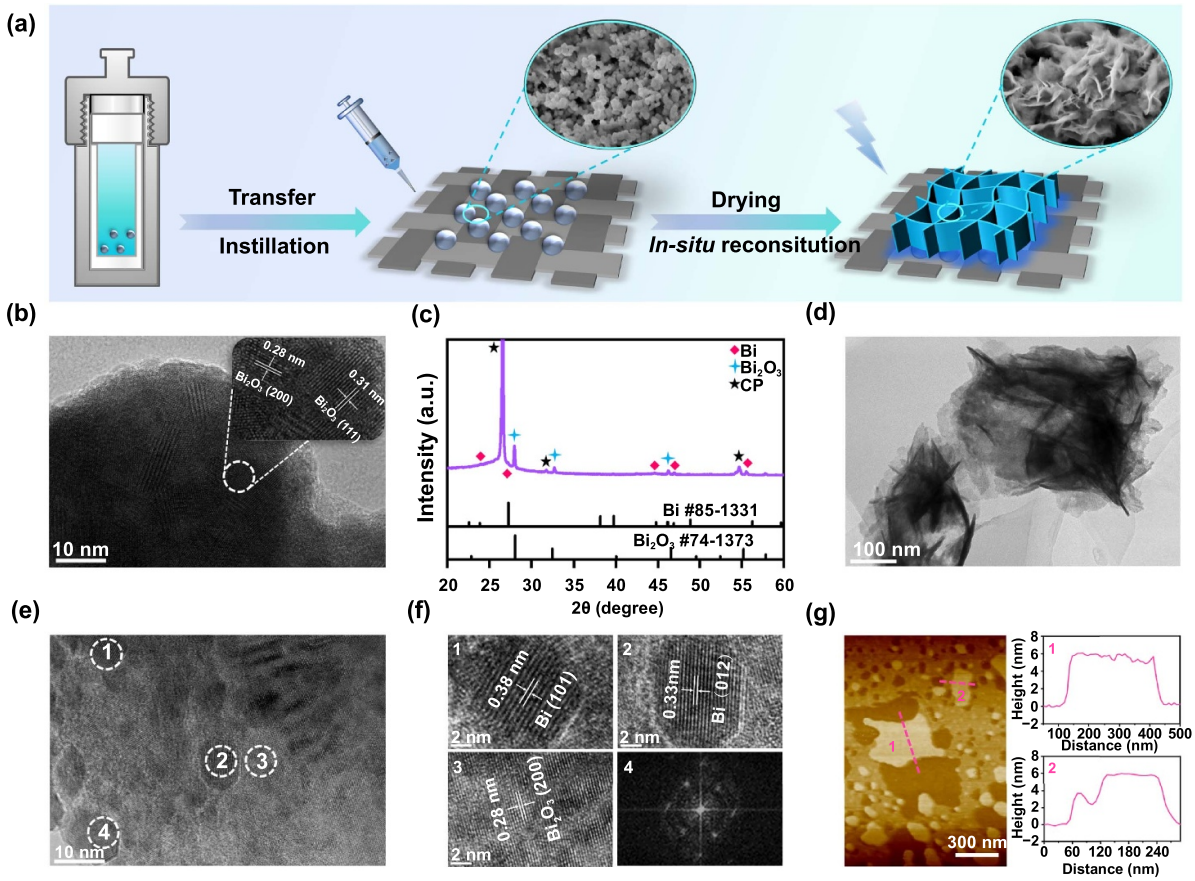

Figure 1. Material characterization related data: (a) synthetic schematic diagram of Bi/Bi_2O_3. (b) TEM and HRTEM (inset) images of Bi_2O_3 NPs. (c) XRD patterns of Bi/Bi_2O_3. (d)–(f) TEM and HRTEM images of Bi/Bi_2O_3. (g) AFM image of Bi/Bi_2O_3.

cathode current (figure S9). A minor damage was found on the morphology of the NSs after the reaction of Bi_2O_3 NSs (figure S10). However, the vibration of Bi–O disappeared after applying a bias voltage. With the increase in the reaction time, the 98 cm^{-1} characteristic peak remained weak (figure S11). Therefore, it can be demonstrated that the quality of Bi crystal was poor, which may have an adverse impact on CO_2RR. In conclusion, the *in-situ* Raman test more clearly showcased the dynamic evolution process of Bi_2O_3 NPs. Also, the transformation from Bi_2O_3 NPs to Bi/Bi_2O_3 NSs was determined in combination with the *ex-situ* test. X-ray photoelectron spectroscopy (XPS) further explained the changes in the elemental composition and valence state of the catalyst surface before and after the electrochemical process. The high-resolution spectrum of Bi 4f (figure 2(c)) showed that the peaks at 164.2 eV and 158.9 eV were assigned to the $Bi^{3+}$of the Bi_2O_3 NPs component. In the deconvoluted Bi 4f spectrum of Bi/Bi_2O_3 after electroreduction, the peaks position at 163.6 eV and 158.3 eV with lower binding energy can be attributed to the generation of metal Bi and oxygen vacancies [33]. In addition, the peaks at 529.5 eV and 531.3 eV in the O1s spectrum of Bi_2O_3 NPs are attributed to the lattice oxygen in Bi–O and the adsorbed oxygen in Bi–OH respectively (figure S12). It is obvious that the ratio of lattice oxygen decreased with the increase of ratio of absorbed oxygen in Bi/Bi_2O_3. Bridging hydroxyl groups were usually associated with surface oxygen vacancies [34, 35], while the Bi–O peak position shifted to the lower binding energy by about 0.1 eV, which also confirms this view [36]. In the meantime, the Mott–Schottky curve (figure 2(d)) also showed a negative shift in the flat band potential (V_{fb}) of the reconstructed Bi/Bi_2O_3, which may be related to the migration of electrons to the Bi surface. The smaller slope of the Bi/Bi_2O_3 curve represented an increase in carrier concentration [2], which indicated that the reconstructed Bi/Bi_2O_3 will exhibits excellent electron transfer capabilities during the CO_2 electroreduction process.

Due to the dynamic evolution of Bi_2O_3 NPs in the electrochemical process (figure S13), the active phase Bi/Bi_2O_3 and stable Bi NPs were used as the main specimens to evaluate the performance of CO_2ERR. The performance indicators of stabilized Bi_2O_3 NSs and commercial Bi powder were also given as a reference (figures S14 and S15). The linear sweep voltammetry curve (figure 3(a)) was measured in 0.5 M $NaHCO_3$ aqueous solution saturated with Ar/CO_2. In the Ar-saturated electrolyte, the HER process occurs; while in the CO_2-saturated electrolyte, the significantly increased current can be attributed to the CO_2RR process. By comparing the current density values, it can be preliminarily concluded based on the result that Bi/Bi_2O_3 has stronger CO_2 reduction ability. Furthermore, the constant potential electrolysis behavior of the catalyst in the CO_2 saturated $NaHCO_3$ solution was also investigated. The gas and liquid

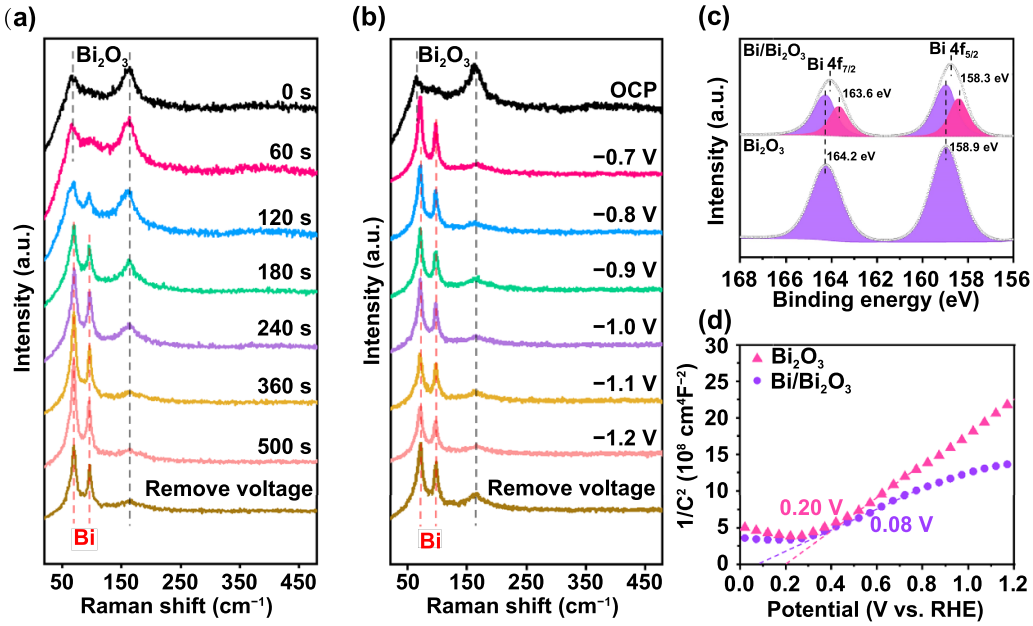

Figure 2. *In-situ* Raman spectroscopy of Bi_2O_3 NPs electrochemical conversion process: (a) Time-dependent Raman spectra at −1.01 V vs. RHE. (b) Potential-dependent Raman spectra, in the CO_2-saturated electrolyte. (c) Bi 4f XPS spectroscopy and (d) Mott–Schottky plots for Bi_2O_3 NPs and Bi/Bi_2O_3.

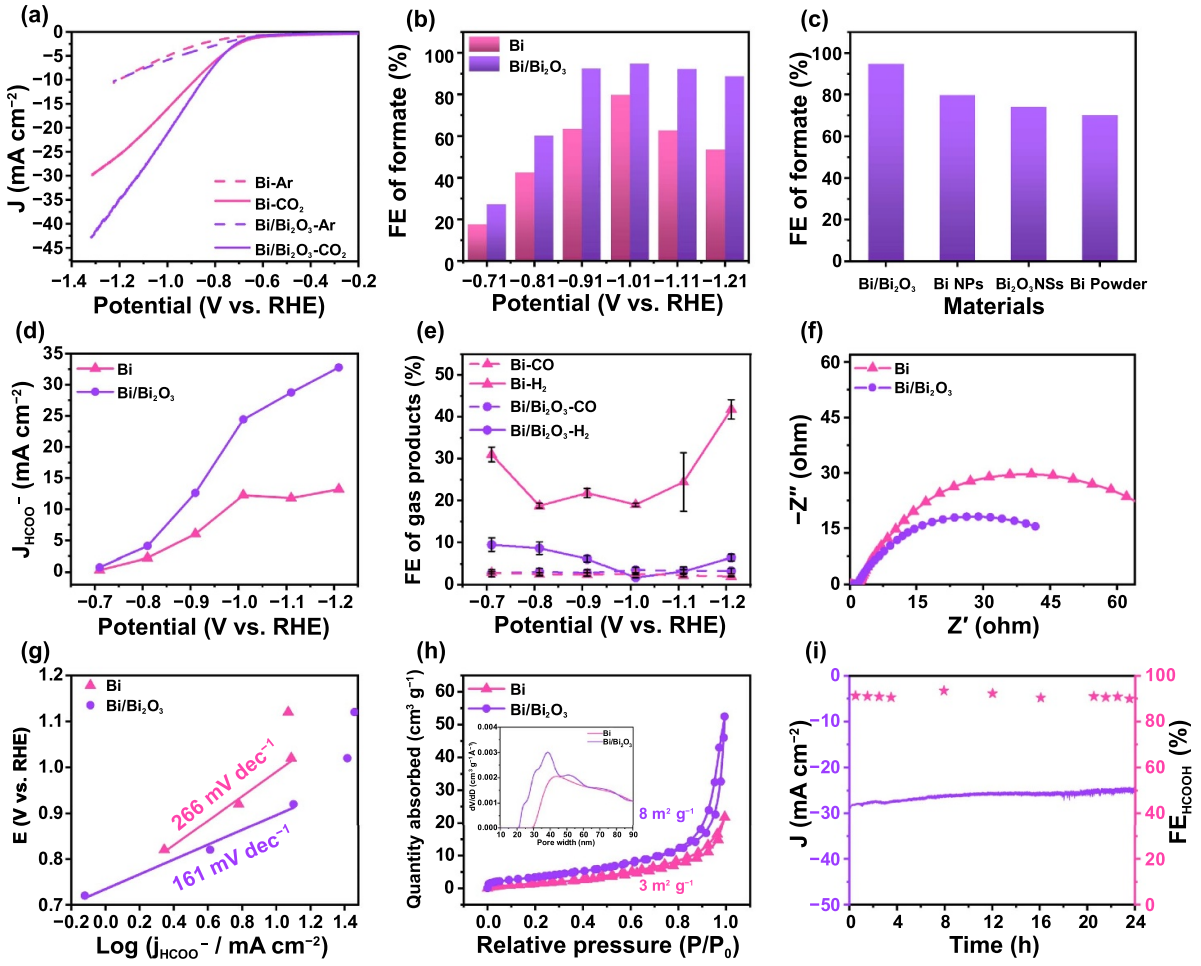

Figure 3. For CO_2RR process data: (a) linear sweep voltammetry curve in 0.5 M $NaHCO_3$ solution saturated with Ar/CO_2. (b) Potential-dependent FE of formate. (c) FE of formate for materials at −1.01 V vs. RHE. (d) Partial-current density of formate. (e) FE of different gas products (H_2, CO). (f) Nyquist plots. (g) Tafel plots of formate. (h) N_2 adsorption/desorption isotherms at 77 K and PSDs (inset). (i) Under −1.01 V vs. RHE, 24 h stability test for Bi/Bi_2O_3.

phase products produced in the cathode compartment were detected by gas chromatography and nuclear magnetic resonance spectroscopy (figure 3(b)). The onset potential of Bi NPs and Bi/Bi_2O_3 for formate production was −0.71 V vs. RHE, while the onset potential of commercial Bi powder was −0.81 V vs. RHE (figure S15). With the increase of applied bias voltage, the Faraday efficiency (FE) of formate increased rapidly; at −1.01 V vs. RHE, the FE of formate for Bi NPs and Bi/Bi_2O_3 reached the maximum value at the same time, which was close to 94.8% and 79.8% with current density ∼26 mA cm^{-2} and ∼14 mA cm^{-2}. The excellent electrochemical performance of Bi/Bi_2O_3 exceeded that of most previous Bi_2O_3 based catalysts (table S1). However, the FE of formate for Bi_2O_3 NSs and Bi powder was only 74% and 70.1%, respectively (figure 3(c)). Subsequently, the FE of formate for Bi NPs dropped rapidly to below 60% after crossing the optimal potential. While the FE of formate for Bi/Bi_2O_3 was still close to 90% at −1.21 V vs. RHE, and remained a high formate selectivity within a large potential window (−0.91 V < E < −1.21 V). The CO_2 reduction ability of the catalysts can be demonstrated more comprehensively by comparing the FE of the main carbonaceous products ($HCOO^-$, CO), which can clearly reflect that Bi/Bi_2O_3 has a stronger CO_2RR efficiency in the potential window involved (figure S16). The potential-dependent formate partial current diagram (figure 3(d)) can clearly show the above changes. A detailed description was provided that the formate partial current of Bi NPs hardly increases after exceeding the optimal potential, whereas Bi/Bi_2O_3 increases slowly. Surprisingly, there was a small amount of acetate in the liquid phase product at a higher potential but further discussion will not be presented in this paper (figure S17). The FE of gas phase product diagram (figures 3(e) and S18) demonstrates the lower CO_2 catalytic ability of Bi NPs due to its prominent HER process. In addition, the reaction kinetics of CO_2RR can be showcased by the Nyquist diagram (figure 3(f)) and Tafel curve (figure 3(g)). It is relatively apparent that the Bi/Bi_2O_3 structure showed a faster electron transport capacity and lower Tafel slope (161 mV dec^{-1}). This supported the conclusion that Bi NPs (266 mV dec^{-1}) need higher overpotential to realize the electron transfer process. At high potential, the higher Tafel slope of catalyst was caused by the low solubility of CO_2 in the electrolyte, which may reach the mass transfer limit in the electrolysis process [37]. The specific BET surface area and electric double-layer capacitance (C_{dl}) also helped support the theory that the Bi/Bi_2O_3 configuration was beneficial for exposing more active areas to participate in the catalytic reaction (figures 3(h) and S19). The stability of the Bi/Bi_2O_3 reaction was further evaluated (figure 3(i)), and the current density remained relatively stable in the 24 h electrolysis test. It is worth noting that there was a slight decrease on the FE of formate, but it still remained above 90%. After the reaction, the catalyst remained relatively stable (figure S20). It is evident that Bi/Bi_2O_3 structure formed *in-situ* by Bi_2O_3 NPs can effectively promote the CO_2RR, and maintain high FE of formate with reasonable stability over a wide potential window.

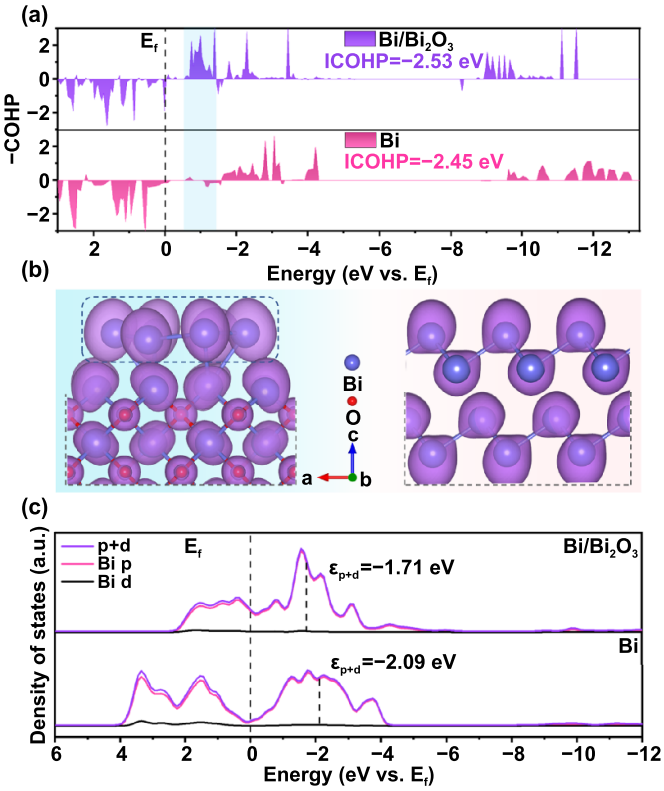

Figure 4. Electronic structure calculation: (a) COHP analysis of the interaction between the Bi atoms. (b) Side-view of ELF on Bi and Bi/Bi_2O_3, with an iso-surface value of 0.004 $eÅ^{-3}$. (c) PDOS on Bi and Bi/Bi_2O_3 calculated by HSE06 hybrid functional; black dotted line marks their band center of active electron density (d band + p band).

In order to explore the origin of the structural stability and the activity of Bi/Bi_2O_3 (figure S21) during the electroreduction, crystal orbital Hamilton population (COHP) analysis (figure 4(a)) was used to study the Bi-Bi bonding state on the catalyst surface by DFT calculation. The region with –COHP greater than 0 represents the bonding state, while the other regions are in the anti-bonding state. The displayed integrated crystal orbital Hamiltonian population (ICOHP) value is integrated up to E_f, which is an effective way to measure the bond strength [38]. As shown in the blue shaded area near the E_f in the figure, the anti-bonding state in the Bi configuration is transformed into a bonding state filled with a large number of electrons in Bi/Bi_2O_3, which is favorable for the bonding between Bi atoms. In contrast, the lower ICOHP (−2.53 eV) delivers a more stable bonding state. It is also consistent with the conclusion of the *in-situ* Raman detection that a stable Bi structure based on Bi_2O_3 is formed during the electrochemical process. Similarly, the adsorption capacity between intermediate and catalyst in the reaction process was closely related to the change of the electronic structure of the catalyst surface, which will significantly affect the catalytic performance. The electron localization function (ELF) can clearly show the localization of the charge around the atom (figure 4(b)). In the Bi configuration, the strong localized charges were spherical around the atoms and have little overlap with the surrounding

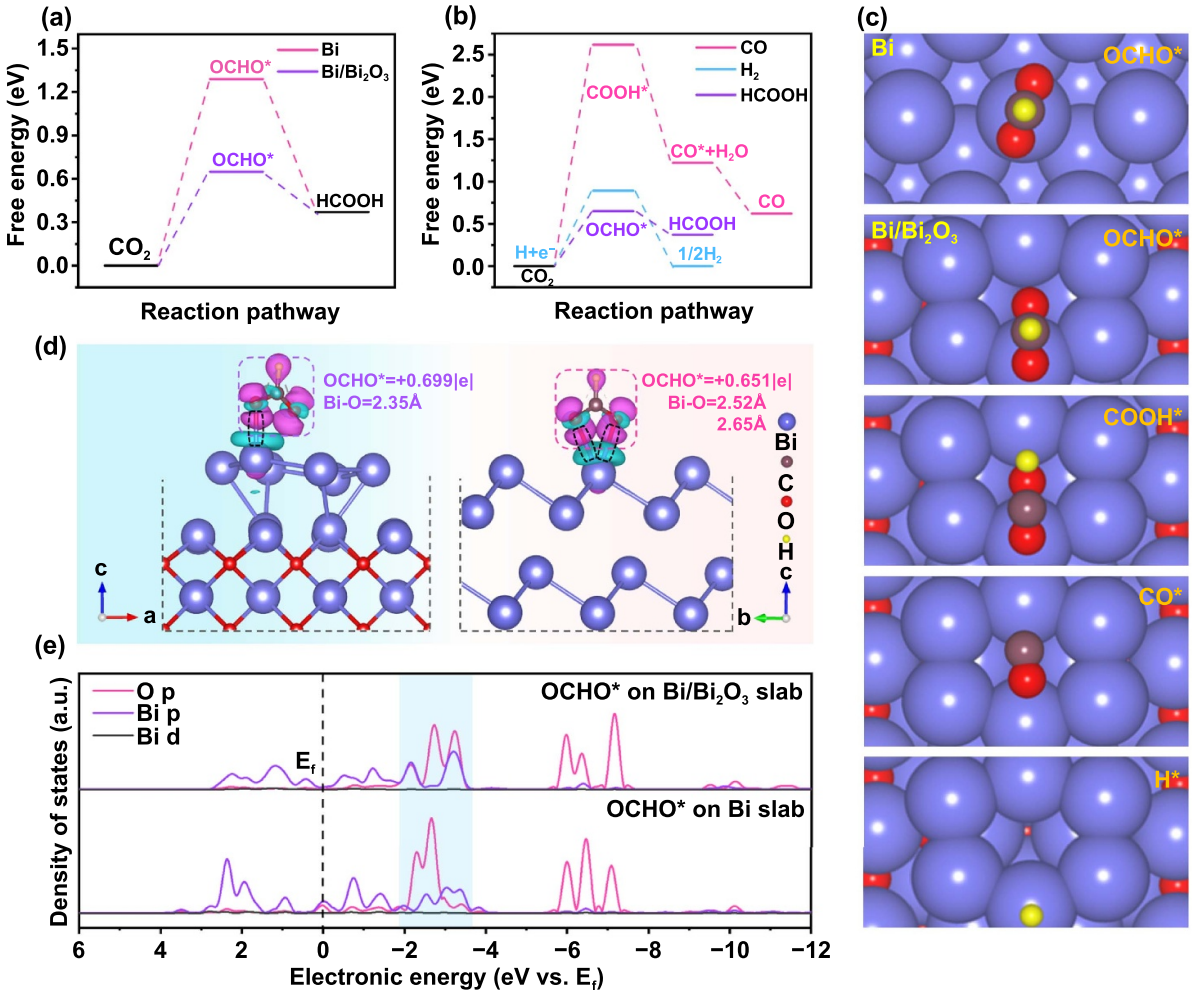

Figure 5. DFT calculation of electrochemical CO_2 reduction process: (a) free-energy profiles of CO_2 reduction pathway to HCOOH for Bi and Bi/Bi_2O_3. (b) free-energy profiles of HER and CO_2 pathways for Bi/Bi_2O_3. (c) The adsorption configuration of the key intermediates involved on the surface. (d) The side-view differential charge density of the $OCHO^*$ on the surface of Bi/Bi_2O_3; purple and dark green corroborate charge accumulation and charge consumption, respectively; the iso-surface value is 0.004 $eÅ^{-3}$; including the bader charge transfer and distance between interface and $OCHO^*$. (e) PDOS of $OCHO^*$ intermediates adsorbed on Bi and Bi/Bi_2O_3 slabs.

atoms. In Bi/Bi_2O_3 configuration, the charges were no longer localized, but instead pulled each other to form a flat ellipsoid. The intercepted 2D picture (figure S22(b)) also demonstrates a similar trend, which represents that charge transfer occurred between the Bi layer and the Bi_2O_3 carrier. Afterward, the surface differential charge density (figure S22(d)) indicates that the outermost Bi atoms in Bi/Bi_2O_3 gained more electrons (0.175 |e|, surface average) from the Bi_2O_3 carrier than the Bi configuration (0.005 |e|), which is consistent with the negative shift in the binding energy of Bi atoms observed in XPS. This suggests that the electron-filled Bi layer in Bi/Bi_2O_3 can become the activity center for the subsequent chemical reaction steps, thereby better promoting the reaction. It is also found that the charge in the Bi/Bi_2O_3 configuration accumulates strongly between adjacent Bi atoms to better facilitate the bonding, which is consistent with the COHP conclusion. Interestingly, the Tafel value of Bi/Bi_2O_3 is closer to 118 mV dec^{-1}, which means that the initial single-electron transfer step CO_2 $^{\bullet-}$ is a rate determining step (RDS) [39, 40] and is closely related to the initial adsorption process of CO_2 molecules on the surface. Consequently, partial density of state (PDOS) (figure 4(c)) of the model was calculated using the hybrid function HSE06 to further explore that the active electron density center of Bi/Bi_2O_3 is closer to the Fermi level (E_f) than Bi. This suggests that the Bi/Bi_2O_3 model has more abundant active states near the E_f, which will contribute to the interaction between CO_2 molecules and the catalyst surface, thereby promoting the charge transfer between each other [41, 42]. In a word, Bi_2O_3 as a catalytically active carrier can adjust the electronic structure state of the surface Bi nanocrystalline to form a more stable surface electronic structure with abundant active electrons, which can help facilitate the interaction between intermediate and catalyst surface to promote the smooth reaction.

The reaction path of CO_2RR was analyzed by DFT calculation to understand the high selectivity of formate for Bi/Bi_2O_3 (figures 5(a) and (b)). The adsorption configurations and Gibbs free energy (G) values of the key intermediates involved were used as a reference (figures 5(c) and S23). For the two-electron process of the HCOOH production

pathway, the first step proton coupled electron transfer of $OCHO^*$ was the RDS in this reaction pathway. The G_{OCHO^*} (0.65 eV) of the Bi/Bi_2O_3 configuration was significantly lower than the G_{OCHO^*} (1.29 eV) of the Bi configuration. The smaller the G was, the higher the product activity was. For further understanding, the differential charge density (figure 5(d)) of the $OCHO^*$ on the catalyst surface indicates that a large number of electrons are consumed between the O atom in $OCHO^*$ and the Bi atom on the catalyst surface, which helps facilitate the bonding and adsorption on the catalyst surface. Compared to the Bi configuration, $OCHO^*$ (0.699 |e|) on the Bi/Bi_2O_3 configuration obtained more electrons and the bond length of Bi–O was smaller (2.35 Å), which is related to the abundant active electrons on the surface (figure S22). For the Bi/Bi_2O_3, the blue shading area in the PDOS (figure 5(e)) indicates that there is a stronger harmonic overlap between the p orbital of the O atom in the $OCHO^*$ and the p orbital of the Bi atom [2]. All results mentioned indicate that the adsorption of $OCHO^*$ on the Bi/Bi_2O_3 surface is tighter, and thereby reducing the over potential of the reaction pathway. Moreover, other competitive reaction paths of Bi/Bi_2O_3 were also calculated (figure 5(b)). It can be clearly demonstrated that $OCHO^*$, $COOH^*$, and H^* are regarded as the RDS affecting the HCOOH, CO, and H_2 reaction pathways. It was difficult to produce CO due to the high G_{COOH^*}. Similarly, G_{H^*} was higher than G_{OCHO^*}, which supports the theory that the HER activity is lower. Finally, the product of the electroreduction reaction can be considered as HCOOH, which is in good agreement with the experimental results and therefore explains the source of the high selectivity of $HCOO^-$. Overall, the Bi/Bi_2O_3 interface optimizes the surface charge to make it easier to contact $OCHO^*$. Therefore, the reaction barrier decreases, and formate becomes the final dominant product.

3. Conclusion

In summary, the dynamic evolution of the Bi_2O_3 NPs in the cathode environment is detected by the *in-situ* Raman spectroscopy. With the 2D trend of the morphology and Bi nanocrystals appearing on the surface, the *in-situ* reconstructed Bi/Bi_2O_3 NSs participate in the CO_2RR process as the real active phase. At −1.01 V vs. RHE, the FE of formate reaches 94.8% and maintains high-efficiency CO_2RR over a wide potential window. The DFT calculation results show that the reconstruction process leads to the accumulation of surface charges, which not only enhances the bonding strength of the surface Bi layer, but also optimizes the absorption of the key intermediate $OCHO^*$ to promote the formation of formate. This work explores the structural evolution of the catalyst under cathode conditions and constructs a model to understand the origin of the activity, which provides a reference for the rational design of the CO_2 reduction electrocatalyst and the future theoretical research of the activity mechanism.

Acknowledgments

Founding: The authors acknowledge the National Natural Science Foundation of China (12025503, U1932134, U1867215 and 12105208), and the Fundamental Research Funds for the Central Universities (2042021kf0068, 2042022kf1181), China Postdoctoral Science Foundation (No. 2020M682469).

The numerical calculations in this paper have been done on the super-computing system in the Supercomputing Center of University of Science and Technology of China.

ORCID iD

Xiangheng Xiao https://orcid.org/0000-0001-9111-1619

References

[1] Chu S, Cui Y and Liu N 2017 The path towards sustainable energy *Nat. Mater.* **16** 16–22
[2] Zhang A, Liang Y X, Li H P, Zhao X Y, Chen Y L, Zhang B Y, Zhu W G and Zeng J 2019 Harmonizing the electronic structures of the adsorbate and catalysts for efficient CO_2 reduction *Nano Lett.* **19** 6547–53
[3] Bushuyev O S, De Luna P, Dinh C T, Tao L, Saur G, Van De Lagemaat J, Kelley S O and Sargent E H 2018 What should we make with CO_2 and how can we make it? *Joule* **2** 825–32
[4] Birdja Y Y, Pérez-Gallent E, Figueiredo M C, Göttle A J, Calle-Vallejo F and Koper M T M 2019 Advances and challenges in understanding the electrocatalytic conversion of carbon dioxide to fuels *Nat. Energy* **4** 732–45
[5] Ross M B, De Luna P, Li Y F, Dinh C T, Kim D, Yang P D and Sargent E H 2019 Designing materials for electrochemical carbon dioxide recycling *Nat. Catal.* **2** 648–58
[6] Yang F *et al* 2020 Bismuthene for highly efficient carbon dioxide electroreduction reaction *Nat. Commun.* **11** 1088
[7] Wang W H, Himeda Y, Muckerman J T, Manbeck G F and Fujita E 2015 CO_2 hydrogenation to formate and methanol as an alternative to photo- and electrochemical CO_2 reduction *Chem. Rev.* **115** 12936–73
[8] Yang H B *et al* 2018 Atomically dispersed Ni(I) as the active site for electrochemical CO_2 reduction *Nat. Energy* **3** 140–7
[9] Lei F C, Liu W, Sun Y F, Xu J Q, Liu K T, Liang L, Yao T, Pan B C, Wei S Q and Xie Y 2016 Metallic Tin quantum sheets confined in graphene toward high-efficiency carbon dioxide electroreduction *Nat. Commun.* **7** 12697
[10] Chen Z P, Mou K W, Wang X H and Liu L C 2018 Nitrogen-doped graphene quantum dots enhance the activity of Bi_2O_3 nanosheets for electrochemical reduction of CO_2 in a wide negative potential region *Angew. Chem., Int. Ed.* **57** 12790–4
[11] Gong Q F *et al* 2019 Structural defects on converted bismuth oxide nanotubes enable highly active electrocatalysis of carbon dioxide reduction *Nat. Commun.* **10** 2807
[12] Liu S B, Lu X F, Xiao J, Wang X and Lou X W 2019 Bi_2O_3 nanosheets grown on multi-channel carbon matrix to catalyze efficient CO_2 electroreduction to HCOOH *Angew. Chem., Int. Ed.* **58** 13828–33
[13] Zhang W J *et al* 2018 Liquid-phase exfoliated ultrathin Bi nanosheets: uncovering the origins of enhanced electrocatalytic CO_2 reduction on two-dimensional metal nanostructure *Nano Energy* **53** 808–16
[14] Zhang S, Kang P and Meyer T J 2014 Nanostructured Tin catalysts for selective electrochemical reduction of carbon dioxide to formate *J. Am. Chem. Soc.* **136** 1734–7
[15] Lei Q *et al* 2020 Investigating the origin of enhanced C_{2+} selectivity in oxide-/hydroxide-derived copper electrodes during CO_2 electroreduction *J. Am. Chem. Soc.* **142** 4213–22

[16] Wu Y S, Jiang Z, Lu X, Liang Y Y and Wang H L 2019 Domino electroreduction of CO_2 to methanol on a molecular catalyst *Nature* **575** 639–42

[17] Zhang A *et al* 2020 *In-situ* surface reconstruction of InN nanosheets for efficient CO_2 electroreduction into formate *Nano Lett.* **20** 8229–35

[18] Han N, Wang Y, Yang H, Deng J, Wu J H, Li Y F and Li Y G 2018 Ultrathin bismuth nanosheets from *in situ* topotactic transformation for selective electrocatalytic CO_2 reduction to formate *Nat. Commun.* **9** 1320

[19] He S D *et al* 2018 The p-orbital delocalization of main-group metals to boost CO_2 electroreduction *Angew. Chem., Int. Ed.* **57** 16114–9

[20] Pang R C, Tian P F, Jiang H L, Zhu M H, Su X Z, Wang Y, Yang X L, Zhu Y H, Song L and Li C Z 2021 Tracking structural evolution: *operando* regenerative CeO_x/Bi interface structure for high-performance CO_2 electroreduction *Natl Sci. Rev.* **8** nwaa187

[21] Chen Y H and Kanan M W 2012 Tin oxide dependence of the CO_2 reduction efficiency on Tin electrodes and enhanced activity for Tin/Tin oxide thin-film catalysts *J. Am. Chem. Soc.* **134** 1986–9

[22] De Luna P, Quintero-Bermudez R, Dinh C T, Ross M B, Bushuyev O S, Todorović P, Regier T, Kelley S O, Yang P D and Sargent E H 2018 Catalyst electro-redeposition controls morphology and oxidation state for selective carbon dioxide reduction *Nat. Catal.* **1** 103–10

[23] Detweiler Z M, White J L, Bernasek S L and Bocarsly A B 2014 Anodized indium metal electrodes for enhanced carbon dioxide reduction in aqueous electrolyte *Langmuir* **30** 7593–600

[24] Jiang H L, Lin Y X, Chen B X, Zhang Y K, Liu H J, Duan X Z, Chen D and Song L 2018 Ternary interfacial superstructure enabling extraordinary hydrogen evolution electrocatalysis *Mater. Today* **21** 602–10

[25] Jiang H L *et al* 2019 Tracking structural self-reconstruction and identifying true active sites toward cobalt oxychloride precatalyst of oxygen evolution reaction *Adv. Mater.* **31** 1805127

[26] Zhu Y P, Wang J L, Chu H, Chu Y C and Chen H M 2020 *In situ*/*operando* studies for designing next-generation electrocatalysts *ACS Energy Lett.* **5** 1281–91

[27] Jiang H L, He Q, Zhang Y K and Song L 2018 Structural self-reconstruction of catalysts in electrocatalysis *Acc. Chem. Res.* **51** 2968–77

[28] Ye K, Zhou Z W, Shao J Q, Lin L, Gao D F, Ta N, Si R, Wang G X and Bao X H 2020 *In situ* reconstruction of a hierarchical Sn-Cu/SnO_x core/shell catalyst for high-performance CO_2 electroreduction *Angew. Chem., Int. Ed.* **59** 4814–21

[29] Steele J A and Lewis R A 2014 *In situ* micro-Raman studies of laser-induced bismuth oxidation reveals metastability of β-Bi_2O_3 microislands *Opt. Mater. Express* **4** 2133–42

[30] Hardcastle F D and Wachs I E 1992 The molecular structure of bismuth oxide by Raman spectroscopy *J. Solid State Chem.* **97** 319–31

[31] Wang Y T, Li Y H, Liu J Z, Dong C X, Xiao C Q, Cheng L, Jiang H L, Jiang H and Li C Z 2021 $BiPO_4$-derived 2D nanosheets for efficient electrocatalytic reduction of CO_2 to liquid fuel *Angew. Chem., Int. Ed.* **60** 7681–5

[32] Mitch M G, Chase S J, Fortner J, Yu R Q and Lannin J S 1991 Phase transition in ultrathin Bi films *Phys. Rev. Lett.* **67** 875–8

[33] Wu D, Huo G, Chen W Y, Fu X Z and Luo J L 2020 Boosting formate production at high current density from CO_2 electroreduction on defect-rich hierarchical mesoporous Bi/Bi_2O_3 junction nanosheets *Appl. Catal.* B **271** 118957

[34] Li L D, Yan J Q, Wang T, Zhao Z J, Zhang J, Gong J L and Guan N J 2015 Sub-10 nm rutile titanium dioxide nanoparticles for efficient visible-light-driven photocatalytic hydrogen production *Nat. Commun.* **6** 5881

[35] Song X Y, He D, Li W Q, Ke Z J, Liu J C, Tang C Y, Cheng L, Jiang C Z, Wang Z Y and Xiao X H 2019 Anionic dopant delocalization through p-band modulation to endow metal oxides with enhanced visible-light photoactivity *Angew. Chem., Int. Ed.* **58** 16660–7

[36] Yang X X *et al* 2020 Partial sulfuration-induced defect and interface tailoring on bismuth oxide for promoting electrocatalytic CO_2 reduction *J. Mater. Chem.* A **8** 2472–80

[37] Rosen J, Hutchings G S, Lu Q, Rivera S, Zhou Y, Vlachos D G and Jiao F 2015 Mechanistic insights into the electrochemical reduction of CO_2 to CO on nanostructured Ag surfaces *ACS Catal.* **5** 4293–9

[38] Zhu M *et al* 2019 Direct atomic insight into the role of dopants in phase-change materials *Nat. Commun.* **10** 3525

[39] Zhang L, Zhao Z J and Gong J L 2017 Nanostructured materials for heterogeneous electrocatalytic CO_2 reduction and their related reaction mechanisms *Angew. Chem., Int. Ed.* **56** 11326–53

[40] Chen Y H, Li C W and Kanan M W 2012 Aqueous CO_2 reduction at very low overpotential on oxide-derived Au nanoparticles *J. Am. Chem. Soc.* **134** 19969–72

[41] Jiang B, Zhang X-G, Jiang K, Wu D-Y and Cai W-B 2018 Boosting formate production in electrocatalytic CO_2 reduction over wide potential window on Pd surfaces *J. Am. Chem. Soc.* **140** 2880–9

[42] He D, Song X Y, Li W Q, Tang C Y, Liu J C, Ke Z J, Jiang C Z and Xiao X H 2020 Active electron density modulation of Co_3O_4-based catalysts enhances their oxygen evolution performance *Angew. Chem., Int. Ed.* **59** 6929–35